POLITECNICO DI TORINO
Repository ISTITUZIONALE

A Structured Methodology to Simulate Composite Advanced Joint Behavior for Ultra-Light Platforms Applications

Original
A Structured Methodology to Simulate Composite Advanced Joint Behavior for Ultra-Light Platforms Applications / Polla, A., Frulla, G., Cestino, E., Das, R., Marzocca, P.. - In: APPLIED SCIENCES. - ISSN 2076-3417. - ELETTRONICO. - 13:2(2023), p. 1004. [10.3390/app13021004]

Availability:
This version is available at: 11583/2974514 since: 2023-01-11T14:26:57Z

Publisher:
MDPI

Published
DOI:10.3390/app13021004

Terms of use:

This article is made available under terms and conditions as specified in the corresponding bibliographic description in the repository

Publisher copyright

(Article begins on next page)

08 June 2026

applied sciences

MDPI

Article

A Structured Methodology to Simulate Composite Advanced Joint Behavior for Ultra-Light Platforms Applications

Alessandro Polla [1,2], Giacomo Frulla [1,*], Enrico Cestino [1], Raj Das [2] and Pier Marzocca [2]

[1] Department of Mechanical and Aerospace Engineering (DIMEAS), Politecnico di Torino, 10129 Torino, Italy
[2] Sir Lawrence Wackett Defence and Aerospace Centre, Aerospace Engineering and Aviation, School of Engineering, RMIT University, Melbourne 3001, Australia
* Correspondence: giacomo.frulla@polito.it

Featured Application: The presented methodology bridges the gap between the numerical evaluation of the specific parameters to fulfil the right physical response of the simulated tests. This provides a more rational approach to the failure simulation of composites, reducing the need for a trial-and-error procedure based on several extensive test campaigns.

Abstract: Numerical simulations have the potential to be used for designing damage-tolerance composite structures. However, numerical models are currently computationally intensive, and their post-failure evolution and fracture morphology predictions are still limited. In the present work, a numerical methodology to simulate advanced composite joints is presented. The results of a numerical campaign aimed to evaluate the progressive damage and failure analysis (PDFA) of an advanced pin-hole connection under tensile and compressive load are evaluated. A high-fidelity stacked shell-cohesive methodology is employed to simulate the ultimate load, fracture initiation, and propagation of the proposed composite joint. Post-failure erosion methodology is proposed to control the initiation and evolution of composite fractures. The location and extension of the numerically predicted damages are compared with experimental observations. The proposed methodology demonstrates its preliminary ability to be used for designing composite joints up to failure. Specific outcomes are also pointed out.

Keywords: fracture mechanics; delamination; cohesive elements; LS-DYNA; advanced joint

Citation: Polla, A.; Frulla, G.; Das, R.; Marzocca, P. A Structured Methodology to Simulate Composite Advanced Joint Behavior for Ultra-Light Platforms Applications. *Appl. Sci.* **2023**, *13*, 1004. https://doi.org/10.3390/app13021004

Academic Editor: Kuo Tian

Received: 29 November 2022
Revised: 20 December 2022
Accepted: 8 January 2023
Published: 11 January 2023

Copyright: © 2023 by the authors. Licensee MDPI, Basel, Switzerland. This article is an open access article distributed under the terms and conditions of the Creative Commons Attribution (CC BY) license (https://creativecommons.org/licenses/by/4.0/).

1. Introduction

Long-endurance ultra-light aircraft have been extensively designed for missions where repetitive actions and permanence on the operative theaters require innovative power balance and regenerative systems. Weight reduction has been considered a design imperative due to the huge lifting surface dimensions required for continuous flight in a day-night scenario [1]. Recently proposed hybrid configurations merged the advanced composite materials with the classical ones for such a demanding design, with the modularity aspects determined by the manufacturing needs. Consequently, a combination of solar power and regenerative fuel cells for long-endurance ultra-light platforms makes composite materials the best candidates for applications where the configuration and shape strictly depend on solar/fuel cell efficiency and weight. Due to the dimensions of long-endurance light vehicles, the focus has been on modular design, another design imperative given the manufacturing limits and for transportability reasons [2–4]. Removable connections fuse mechanical bolted joints, but in the case of carbon fiber-reinforced polymers (CFRP), the best structural efficiency is managed by a proper design configuration to increase the maximum allowable bearing failure limit. Removable connections request the following main aspects: (a) defined load distribution between different primary structural parts according to the airworthiness safety-oriented indications; (b) fast assembly and dismounting

without any permanent effects on the materials; (c) easy and correct positioning of the different structural parts demonstrating the right clearance and tolerance limit. Stress distribution around holes in anisotropic composite plates subjected to specific loading combinations is well understood; e.g., [5,6]. However, damage in a composite joint can initiate at an early stage and accumulate inside the laminate as the load increases. Different failure modes depend on the choice of material, ply stacking sequence, laminate thickness, joint geometry, edge effects, and bearing and clamping effect, all based on the applied loading conditions. The validation and verification of the structural sizing of such composite joints is carried out using a combination of experimental tests and static numerical analysis. Nevertheless, the evaluation of failure and post-failure modes is frequently excluded from numerical studies. Typically, designers tend to increase experimental investigations to reconstruct the failure modes of a composite structure according to normative [7]. The lack of a fully validated and standardized numerical tool has become fundamental in the preliminary design procedure, especially for the design of composite structures subjected to specific critical loads. These tools are requested to accurately and reliably predict physical response when damage is initiated and failure mechanisms start, as described in [6–10]. Referring to the experimental activities described in Frulla et al. [2] at Politecnico di Torino under the "HELINET" project, a structured comparison between the numerical results and the experimental observations is proposed here. The experimental joint configuration is based on a solid or sandwich CFRP laminate with the same lay-up loaded in two different structural configurations: (a) basic laminate joint, (b) innovative joint configuration ("advanced joint" in the following) completed with a steel reinforcement at the hole position specifically designed to overcome the bearing failure mode of a composite laminate (see Figure 1).

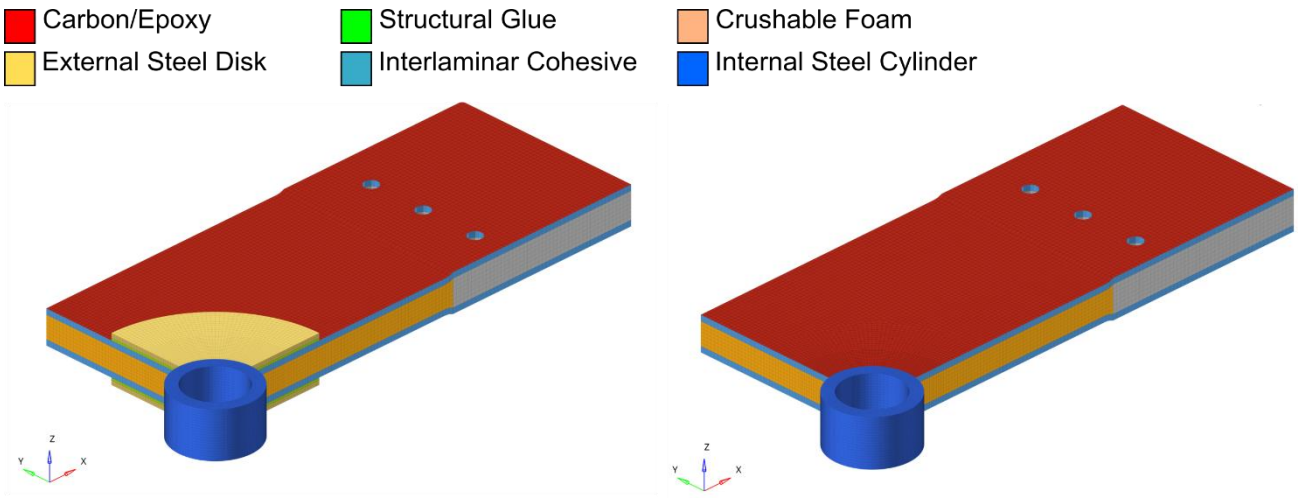

Figure 1. Section of proposed composite joint configuration: (SX) Advanced Joint; (DX) Simple Joint.

High-fidelity new shell-cohesive progressive damage failure analysis (PDFA) methods, different with respect to the solid-cohesive one as reported in the open literature and described in Section 3, have been proposed to numerically reconstruct the performances of specified sandwich sample structural configurations under tensile and compression loading conditions. A complete stacked shell modeling technique, as described in Polla et al. [11], with the application of specific material models available in the LS-DYNA software package was applied. A cohesive zone model (CZM) was introduced to describe the delamination evolution in the proposed composite joint configurations under different critical loads. Material formulations in LS-DYNA were compared in [12] and a consistent selection is proposed here. The presented numerical results are validated against simple experimental data to support modeling features, such as observed deformations and physical modes of failure. The described results also present the possibility to generalize

the modeling methodology to complex geometrical composite configurations as a consequence of this research activity.

2. Advanced Joint Configuration

A flat sample configuration was chosen for rapid execution of the related testing activities even though the real joints were positioned on a cylindrical surface, as in Figure 2. Such a real mounting configuration was tested during the full-scale bending-shear test of the HELIPLAT prototype, as in [13], confirming the validity of the selected experimental campaign as described in the following sections. Two specific experimental configurations were proposed: a sandwich joint configuration with a 9 mm core-thickness of standard Rohacell 51 rigid foam reinforced with glass microspheres, and a solid sample with the same lay-up. The sample dimensions were 240-mm-long, 130-mm-wide with an active zone of damage around the hole of 170-mm-long and 130-mm-wide. The preliminary design of a composite joint typically starts with the definition of the correct laminate lay-up and material selection. According to [2], all of the evaluated samples tested in the experimental campaign were manufactured with the same Uni-Directional (UD) M40J/epoxy material and the same laminate lay-up $[+20/-20/90/45/-45/90/45/-45]_s$ for every single skin, which maximizes laminate bearing strength (Figure 3), avoiding net-tension/shear-out failure. The nominal thickness of a single composite laminate is 2.16 mm, and the approximate thickness of a single lamina is around 0.135 mm. The mechanical properties of the adopted materials are reported in Tables 1–3. The advanced composite joint is reinforced with two steel plates (yellow part in Figure 3) with an external diameter of 80 mm and a thickness of 1.5 mm. The internal steel cylindrical support connected to the flat external steel plates has an internal diameter of 20 mm and a thickness of 3.95 mm. The reinforcement is bonded to the composite laminate by means of Araldite adhesive, as detailed in Table 3 and as shown in Figure 4 (green layer). The internal cylinder provides the loading transmission between the joint structure and the bolt during the pin-loaded test. The relative positions of the Strain-Gauge (SG) are reported in Figure 3 according to [2]. Experimental static properties for the proposed flat configurations are summarized in Table 4 [2]. The load was applied up to sample failure to understand the modes of fracture and the improvement obtained with the advanced configuration. The experimental results show a reduced capacity of the simple solid and sandwich configuration to overcome the typical 20 kN pin bearing load. The average failure load for the solid composite joint was about 20,481 N and 39,481 N for the sandwich configuration.

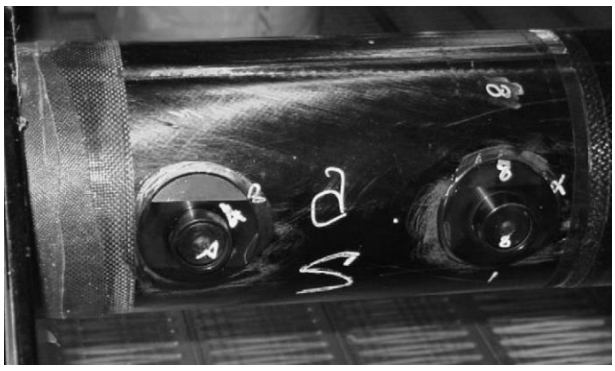

Figure 2. "HELINET" project prototype connection detail.

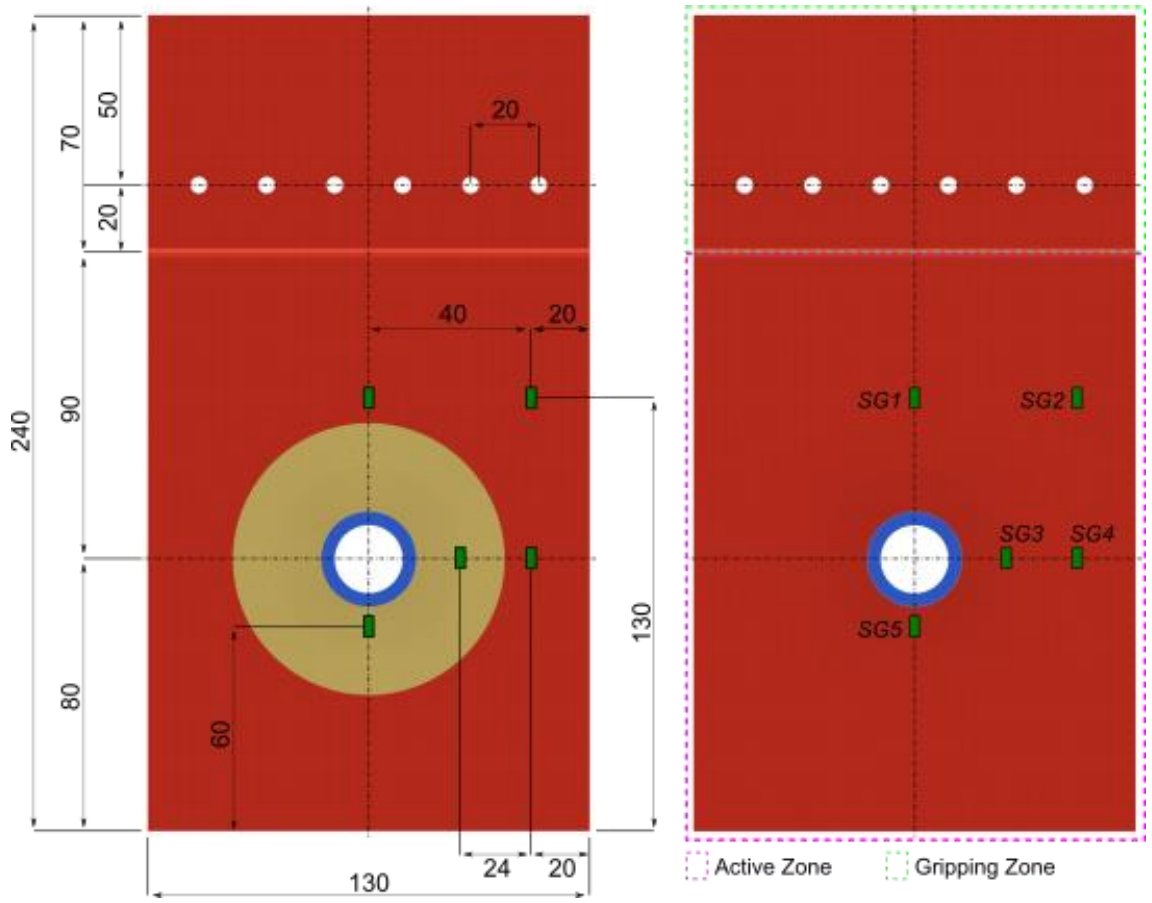

Figure 3. Sample dimension and SGs position [mm].

Table 1. Stiffness material properties of M40J/epoxy as published in Frulla et al. (*) [2] and associated strength material threshold [14].

Property	Units	Symbol	LS-DYNA Parameters	Experimental Value
Density	[kg/mm³]	ρ	RHO	1.6×10^{-6} *
Modulus *1-direction*	[GPa]	E_1	EA	215.0 *
Modulus *2-direction*	[GPa]	E_2	EB	66.7 *
Shear modulus *12-direction*	[GPa]	G_{12}	GAB	4.3 *
Shear modulus *23-direction*	[GPa]	G_{23}	GBC	3.6 *
Shear modulus *31-direction*	[GPa]	G_{31}	GCA	3.6 *
Major Poisson's ratio	[-]	ν_{12}	-	0.27 *
Minor Poisson's ratio	[-]	ν_{21}	PRBA	0.0837
Strength *1-direction tension*	[GPa]	σ_{11}^T	XT	2.365
Strength *2-direction tension*	[GPa]	σ_{22}^T	YT	0.072
Strength *1-direction compression*	[GPa]	σ_{11}^C	XC	1.270
Strength *2-direction compression*	[GPa]	σ_{22}^C	YC	0.140
Shear strength *12-direction*	[GPa]	τ_{12}	SC	0.063

Table 2. Material properties of Rohacell 51 [15].

Property	Units	Symbol	LS-DYNA Parameters	Experimental Value
Density	[kg/mm³]	ρ	RHO	5.2×10^{-8}
Elasticity modulus	[GPa]	E	E	0.0686
Major Poisson's ratio	[-]	ν_{12}	PR	0.05
Minor Poisson's ratio	[GPa]	σ_Y	TSC-SIGP1	0.00186

Table 3. Material properties of Araldite adhesive [16].

Property	Units	Symbol	LS-DYNA Parameters	Experimental Value
Density	[kg/mm³]	ρ	RHO	8.0×10^{-7}
Elasticity modulus	[GPa]	E	E_N	1.7
Elasticity modulus	[GPa]	G	E_T	0.8
Energy release rate I	[GPa×m]	GIC	GIC	1.10×10^{-3}
Energy release rate II	[GPa×mm]	$GIIC$	GIIC	1.45×10^{-3}
Tensile strength	[GPa]	σ^T	T	0.041

On the other hand, the advanced configuration average failure load was about 94,267 N for the solid sample and 97,363 N for the sandwich one. The mode of failure changes from the typical bearing failure related to a simple solid/sandwich joint to a standard tension failure mode outside the joint position for the advanced configuration confirming the well-behaved design of such a solution (Figure 5). Such experimental results have been used as a benchmark in comparing and correlating the numerical methodology proposed in the following sections. The primary objective was to characterize and reproduce the mechanical behavior of the sandwich flat samples with the adoption of an explicit LS-DYNA R11.1 solver [17,18]. In particular, the results are focused on calibrating and verifying the sandwich composite joint FE explicit numerical model against the experimental evidence. Subsequently, a reproduction of the failure mode mechanism has been determined. The cylindrical arrangement has been left to future investigation.

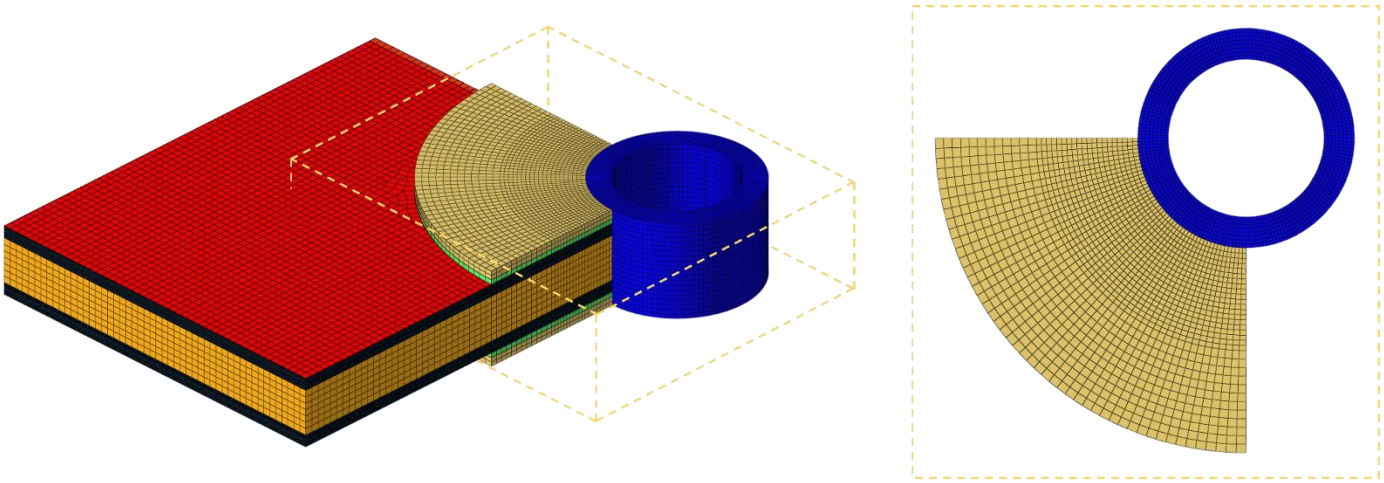

Figure 4. Characteristic section of the composite sample and structured mesh details inserted around the pin-hole in both advanced and simple configurations.

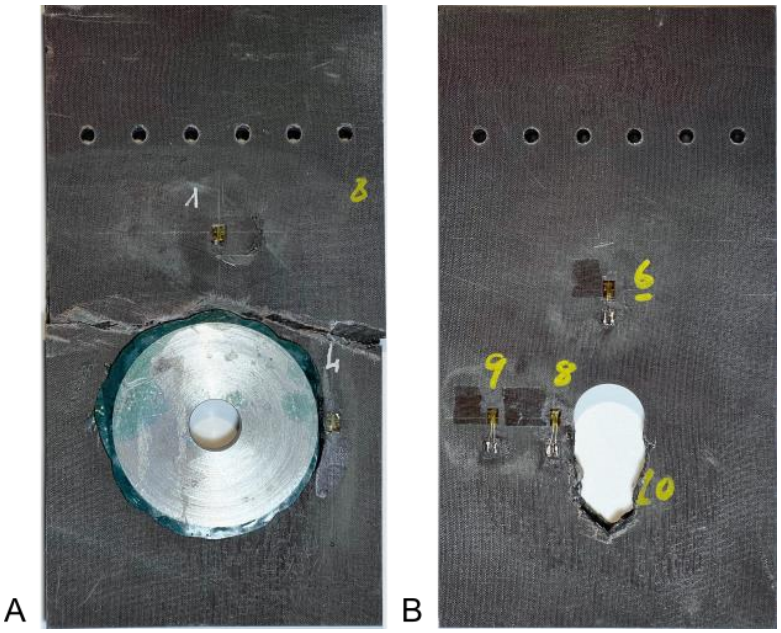

Figure 5. Experimental failure modes: (**A**) for the advanced joint, (**B**) for the not reinforced joint. A similar failure mode has been determined for the solid configuration.

Table 4. Experimental static failure load for different CFRP samples in initial and advanced configuration (A-i = solid laminate; B-i = sandwich laminate).

Sample	Not Reinforced [N]	Reinforced [N]
A-01	21,327	93,862
A-02	21,401	93,646
A-03	18,714	95,294
B-01	39,326	97,971
B-02	37,500	98,924
B-03	41,618	98,193

3. Numerical Modeling Methodology of Composite Advanced Joint

Several numerical techniques have been proposed in the literature for reproducing the orthotropic nature of composite materials [19–22]. Recently, many numerical applications have been based on a ply-by-ply modeling technique of composite structures with the adoption of solid Hexa FE elements. Gomez et al. [23] modeled a composite-fastener joint with one through-thickness solid element for each composite ply. The proposed model was based on the application of the calibrated LS-DYNA material model MAT162 extracted from the preceding phase of the NASA ACC HEDI project [8,9]. Moreover, Girolamo et al. [24] proposed the same FE modeling technique to predict the strength of a composite-bonded joint under longitudinal tensile loads. However, the applicability of a ply-by-ply solid model is restricted to small samples and requires high computational resources. Finally, Gerendt et al. [25] presented an FE model to predict the static progressive failure behavior of fiber metal-laminated bolted joints. A user-defined continuum-damage constitutive model was formulated and applied to a ply-by-ply solid numerical model. A complete stacked shell modeling technique (L2DE-Cohesive), proposed and described by Polla et al. [11], was considered for the present evaluation and it was validated against experimental evidence of a complex sandwich structure subjected to critical tensile loads. A shell-cohesive modeling approach can be considered to be a new and substantial step in simulating composites by means of LS-DYNA application, different with respect to the usual solid-cohesive procedure. Computational cost reduction and the possibility to simulate composites in a macro-scale environment can be viewed as an interesting

consequence of this modeling technique. A brief description of such a modeling technique is summarized in the following paragraphs, as derived by [14] and presented in Figure 6.

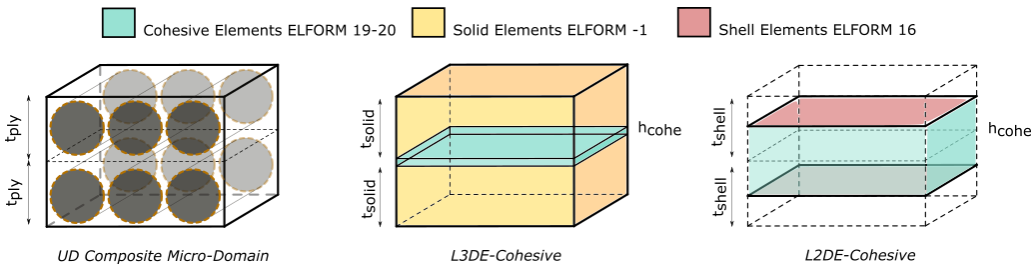

Figure 6. Schematic representation of different FEM-Cohesive models [11].

A single plane of 2D shell elements was introduced for each composite ply belonging to the laminate. The two-dimensional elements plane belonging to a single ply was placed at the geometric mid-surface of each physical composite layer. *PART_COMPOSITE was chosen to define each shell-ply that constituted the composite laminates. Structural continuity through the thickness was established with the application of interlaminar interface elements (CZM) properly connected node-to-node to the adjacent ply mesh structure. The introduction of defined cohesive elements restored the structural integrity and allowed the definition of transverse stiffness and toughness associated with the specific composite material [11]. ELFORM 20 cohesive formulation was applied for compatibility with a selected two-dimensional adjacent mesh.

Solid metallic components, crushable core foam, and composite gripping sections were represented with solid Hexa FE elements. A fully-integrated shell element formulation (ELFORM 16) was selected to avoid energy dissipation from hourglass modes. Three integration points (IP) were defined through the thickness of each composite layer to correctly reproduce possible bending deformation modes in every single ply. An efficient fully-integrated solid element formulation (ELFORM-1) was selected for all solid-modeled components. A structured circular mesh was refined as the periphery of the bolt was approached to improve the aspect-ratio index of finite elements and improve energy conservation during the high-deformation fracture process observed in the experimental tests. A characteristic mesh length parameter was set between 0.35–1.4 mm (Figure 1) according to a previous FE evaluation, see [3,4]. A finer mesh was applied around the circular hole region, pointing out stress variations around the hole (Figure 4).

The reported mesh-length parameter was derived by the static stress and strain distribution around the pin-loaded point when compared to previous analyses and experimental tests. Reference to previous convergence evaluations was assumed enough for this research activity avoiding repetitions. Furthermore, the post-failure regime could be dependent on several cohesive parameters avoiding a direct convergence investigation. For this reason, a pre-failure numerical/experimental comparison was considered representative for the presented research; similar to different element type selection. An LS-DYNA *CONTACT_SINGLE_SURFACE algorithm was employed to define ply-to-ply post-failure interaction and to reproduce the Coulomb friction that exists between delaminated ply interfaces. Both static and dynamic composite coefficients of friction were equally set to 0.2 and a viscous damping coefficient of 0.05 for the critical factor was introduced. Moreover, a contact surface algorithm was introduced to reproduce the load exchanged in the hole between the cylindrical steel support and the sandwich structure during the control displacement loading. In particular, an automatic contact algorithm was introduced (*CONTACT_AUTOMATIC_NODE_TO_SURFACE) to model this interaction. During fracture propagation, the initial contact surface can progressively change; for this reason, a set of slave nodes around the hole was selected to interact with a master rigid contact surface associated with the external steel cylinder. For example, one-quarter of the selected sandwich FE node set is represented in the yellow dotted box in Figure 4. Classic

Coulomb coefficients of friction were set to 0.16 for the static and 0.11 for the dynamic conditions. A viscous damping coefficient was introduced for this contact equal to 0.05 to control the damp energy inside the numerical model and reduce the high-frequency modes associated with the fracture propagation. A soft constraint algorithm (SOFT 1) was set for both contact algorithms. Contact parts were represented in [12] with the characteristic distinction between master and slave groups. Moreover, the *CONTACT_INTERIOR algorithm was inserted to avoid the negative volume of crushable solid foam elements when subjected to compression loads. Single point constraints (SPC) were applied to the six-aligned holes in the gripping area. Constrained xyz-displacements were set to all the through-thickness FEA nodes that constitute the aligned holes in the Gripping Zone reported in Figure 3. Prescribed displacement was applied to the rigid cylindrical internal steel support to generate the requested tension load.

The simulations were executed on LS-DYNA R11.1 explicit single-precision MPP solver. One node on an HPC architecture with Intel Xeon Gold 6130 16 cores was adopted. Sandwich FE models with metallic circular flat support had 873,318 nodes, 832,596 solid elements, and 661,632 shell elements. On the other hand, the sandwich model without the metallic support plate had 836,454 nodes, 795,732 solid elements, and 661,632 shell elements. Every simulation was completed in a mean of 10 hours.

4. Material Model for Progressive Damage Failure Analysis of Composite Structure

Composite structures have the potential to exhibit different and simultaneous failure mechanisms when subjected to multiple loading conditions. Tensile and compressive fiber fracture, intralaminar matrix fracture within CFRP plies, delaminations between adjacent plies, adhesive debonding, sandwich core crushing, etc. All these failure mechanisms interact and influence the final failure mode of the evaluated composite sample. No strain-dependent material properties were evaluated in this research activity. Multiple intralaminar material models are available and different numerical methodologies can be selected to reproduce the composite elastic and fracture evolution in LS-DYNA [17]. The presented research focused on the material formulation defied by the MAT58 scheme according to Matzenmiller et al. [26] and related to the composite laminate simulation. MAT58 defines a smooth stress-strain relation and implements classic Hashin failure criteria to control the failure initiation inside a specific element. An effective strain parameter (ERODS) is used to control the erosion of FE elements inside this numerical model during a post-failure condition. Post-failure softening values can be defined in the described material model to manage the residual strength of selected material directions (SLIMxx). Moreover, a detailed application of several composite material models was reported in [12]. Material and numerical parameters obtained through a calibration process and adopted in the selected composite material formulation are proposed in Table 5.

Table 5. MAT58 intralaminar numerical parameters.

Variable	Definition	Inserted Value
SLIMT1	Post failure maximum stress limit 1-tension	0.25
SLIMT2	Post failure maximum stress limit 2-tension	0.90
SLIMC1	Post failure maximum stress limit 1-compression	0.45
SLIMC2	Post failure maximum stress limit 2-compression	0.90
SLIMS	Post failure maximum plane stress shear direction	0.90
TFAIL	Time step criteria for element deletion	1.0×10^{-8}
ERODS	Maximum effective strain for element failure	−0.3
E11C	Strain at longitudinal compressive strength	0.0065
E11T	Strain at longitudinal tensile strength	0.012
E22C	Strain at transverse compressive strength	0.00231
E22T	Strain at transverse tensile strength	0.0012
GMS	Engineering shear strain at shear strength	0.03144

The Cohesive Zone Model (CZM) is a mathematical technique that tries to represent the stress-displacement relation that exists around an initiated material crack. The CZM method is based on a nonlinear numerical procedure that consists of reproducing the initiation and evolution of cracks or delaminations in a known a priori propagation path. A characteristic bi-linear cohesive curve is described in terms of local stress versus crack opening displacement Figure 7.

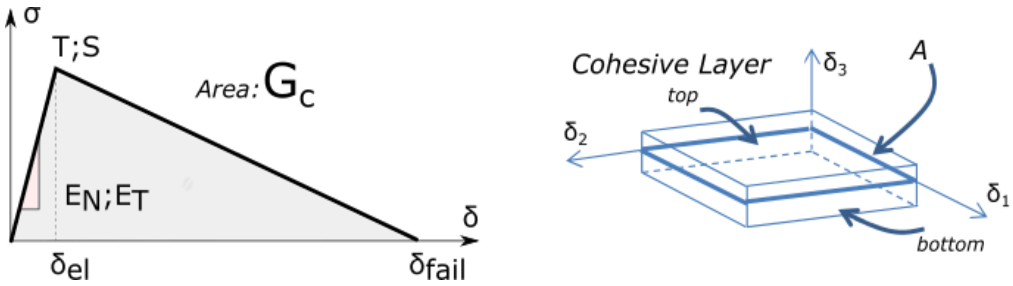

Figure 7. Cohesive constitutive law-bilinear shape; schematic cohesive element representation with the definition of constitutive displacement relative to the top and bottom surface of adjacent shell layers.

Fracture surface initiates inside a cohesive zone only upon satisfaction of characteristic failure strength. After failure initiation, the stiffness properties of damaged elements soften with further deformation. The area underneath the CZM constitutive law defines the energy necessary to propagate the fracture, which is commonly associated with fracture toughness (G_C). *MAT_COHESIVE_MIXED_MODE (MAT138) was selected for the definition of the CZM elements in the interlaminar region between adjacent composite plies. Cohesive material properties and cohesive stiffness values obtained with the formulations proposed by Polla et al. [11] are reported in Table 6.

Table 6. MAT138 material parameters for the interlaminar region.

Variable	Definition	Inserted Value
RHO-[kg/mm²]	Mass per unit volume	8×10^{-7}
ROFLG	Density per unit of volume or area	1.0
INTFAIL	N° Integration point for deletion of an element	1.0
EN-[GPa/mm]	Normal cohesive stiffness	28.2
ET-[GPa/mm]	Tangential cohesive stiffness	16.0
GIC-[GPa×mm]	Energy release rate for mode I	3.52×10^{-4}
GIIC-[GPa×mm]	Energy release rate for mode II	1.45×10^{-3}
XMU	Exponential of the mixed mode criteria	−1.0
T-[GPa]	Peak traction in the normal direction	0.050
S-[GPa]	Peak traction in the tangential direction	0.092

Crushable closed-cell foam core shows fragile behavior in tension and non-linear evolution in compression. *MAT_CRUSHABLE_FOAM (MAT63) was selected to numerically reconstruct the physical behavior of closed-cell foam Rohacell 51 used in the advanced joint sandwich samples. MAT63 is dedicated to modeling crushable foam with optional damping and tension cutoff reconstructing its compressive crushable behavior. A Rohacell 51 characteristic curve based on mechanical material properties was defined by a specific MATLAB code according to standard behavior derived from the literature. Moreover, a *MAT_ADD_EROSION card was inserted to define tensile stress failure and erosion control parameters for the solid foam FE elements. Mechanical parameters and numerical values adopted for this formulation are reported in Table 7.

Table 7. MAT63 material properties for crushable closed-cell foam.

Variable	Definition	Inserted Value
RHO-[kg/mm²]	Mass per unit volume	5.2×10^{-8}
E-[GPa]	Young modulus	0.0686
PR	Poisson ratio	0.05
TSC-[GPa]	Tensile stress cutoff	0.00186
EFFEPS	Maximum effective strain for element erosion *MAT_ADD_EROSION	0.5
VOLEPS	Volumetric strain at failure *MAT_ADD_EROSION	−0.5
NUMFIP	Percentual number of failed integration points *MAT_ADD_EROSION	−100
SIGP1-[GPa]	Principal stress at failure *MAT_ADD_EROSION	0.00186

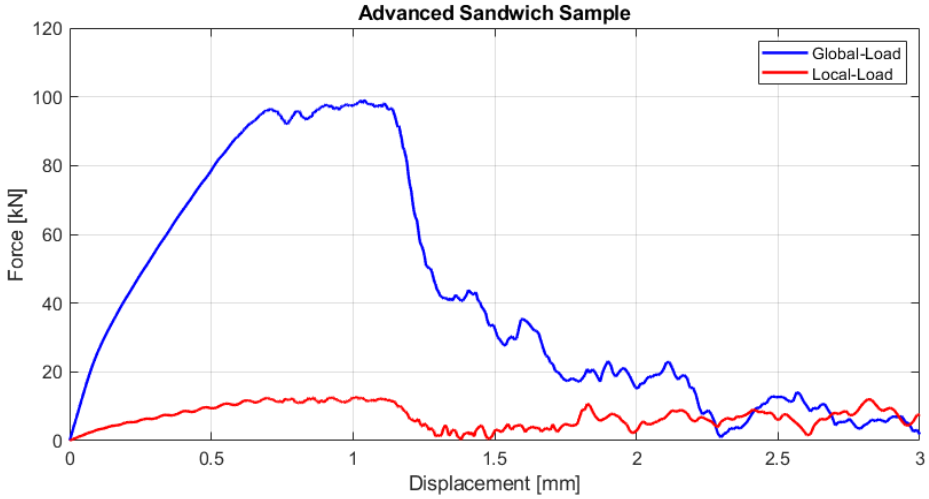

Figure 8. The characteristic force-displacement curve for the advanced composite joint.

5. Numerical and Experimental Results

The selected joint configurations were investigated and numerically simulated with the introduced material models based on the LS-DYNA procedure previously described, under a static pin-loaded tension test for experimental/numerical comparison and validation. The predicted peak loads of the composite specimens are listed in Tables 8 and 9 and corresponding force-displcement curve are shown in Figures 8 and 9. Moreover, the fracture morphology numerically reproduced for both the proposed composite samples is reported in Figures 10 and 11. The intralaminar composite material models available in current numerical solvers are typically defined with the application of two macro sections: the undamaged elastic region and the damaged region. The passage from one region to the adjacent one is typically controlled by strength-based failure criteria specifically associated with the selected material formulation. The damaged region related to MAT58 card is generally described with the introduction of two characteristic values: SLIM$_{XX}$ and ERODS. SLIM$_{XX}$ is related to the post-failure residual strength for each orthotropic material direction, while a single ERODS value is connected to the FE-element erosion during fracture initiation/propagation during numerical simulation. The MAT58 erosion parameter was calibrated at an absolute value of about 0.3, following the full tensorial formulation available in LS-DYNA (ERODS < 0 option). The same calibrated value was adopted for the advanced joint configuration and for the simple one. The calibrated value and its

related numerical results were compared and discussed against the experimental evidence reported in Frulla et al. [2].

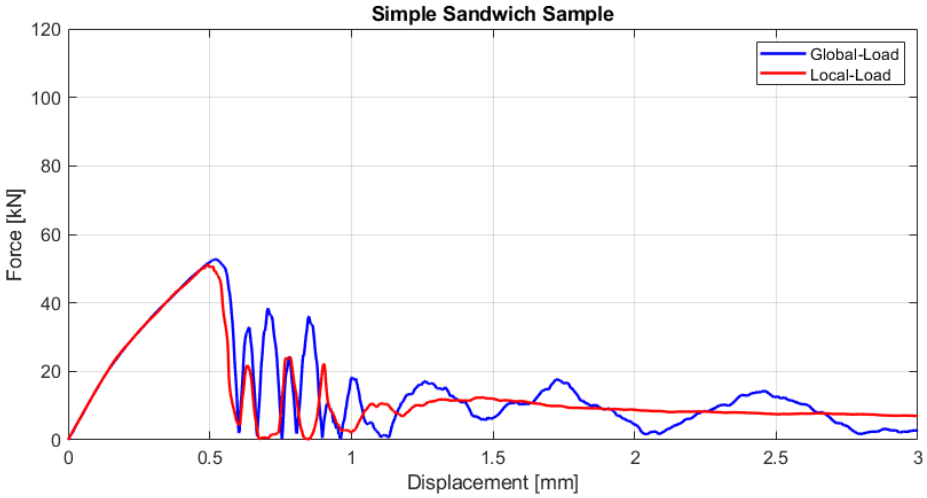

Figure 9. The characteristic force-displacement curve for the simple composite joint.

The characteristic force-displacement curve of the advanced composite joint is reported in Figure 8. There are two different curves: the blue curve represents the tensile load evolution in the function of the pin displacement; the red curve describes the contact load exchanged between the external rigid steel surface of the cylinder and the internal surface of the sandwich hole with respect to the global pin displacement. Both curves can be divided into three characteristic zones: (a) the first elastic part that describes the nonlinear evolution of the loading inside the composite structural joint; (b) the second part of the curve that represents the initiation of the failure; (c) the third part that shows the fracture evolution process inside the entire specimen. For the advanced joint case, the curve is characterized by two distinct peaks in the failure zone. The first peak represents the initiation of failure inside the composite joint; instead, the second strength limit defines the failure of the entire sample and the beginning of the global fracture process. The load difference between the global failure point (blue curve) and the maximum internal contact force (red curve) is equally distributed around the hole by the presence of the steel circular plate, characteristic of the advanced composite joint. The fracture surfaces reported in Figure 10 show that the principal failure mode for the advanced composite joint is a pure complete tensile load. It shows a satisfactory correspondence with the experimental evidence, as indicated in Figure 5A, demonstrating the validity of the presented methodology in simulating such failure conditions.

Table 8. Reinforced maximum load comparison.

Source	**Reinforced Sample [kN]**		
Experimental Sample		97.3	
LS-DYNA Model	First Peak [kN]	Second Peak [kN]	ERR [%] (Max Peak)
MAT58_MAT63	96.3	98.5	1.1

Table 9. Not reinforced maximum load comparison.

Source	**Not Reinforced Sample [kN]**		
Experimental Sample		39.5	
LS-DYNA Model	First Peak [kN]	Second Peak [kN]	ERR [%] (Max Peak)
MAT58_MAT63	52.7	-	25.1

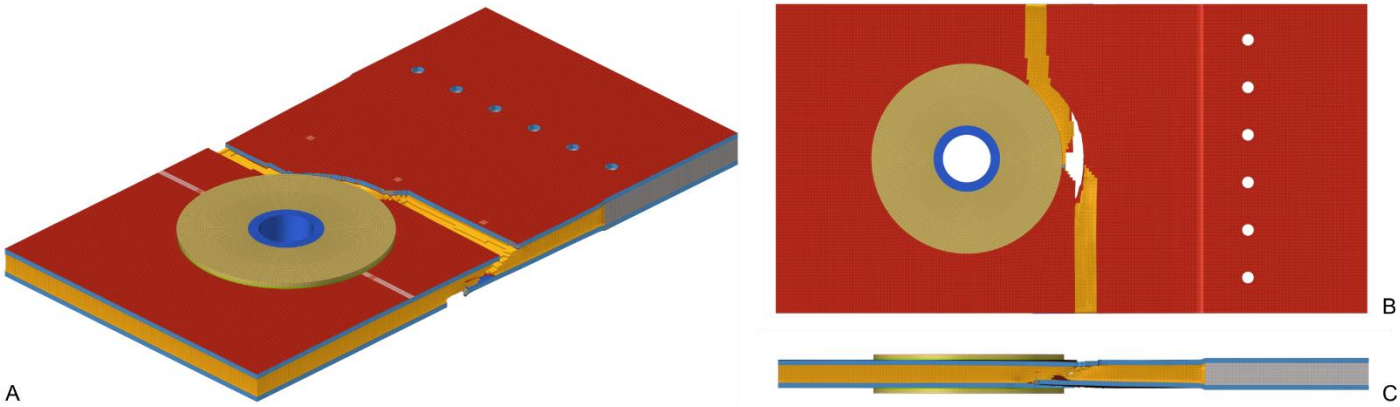

Figure 10. The numerical fracture surface of advanced composite joint model. (**A**) Fracture axonometry. (**B**,**C**) Fracture surface.

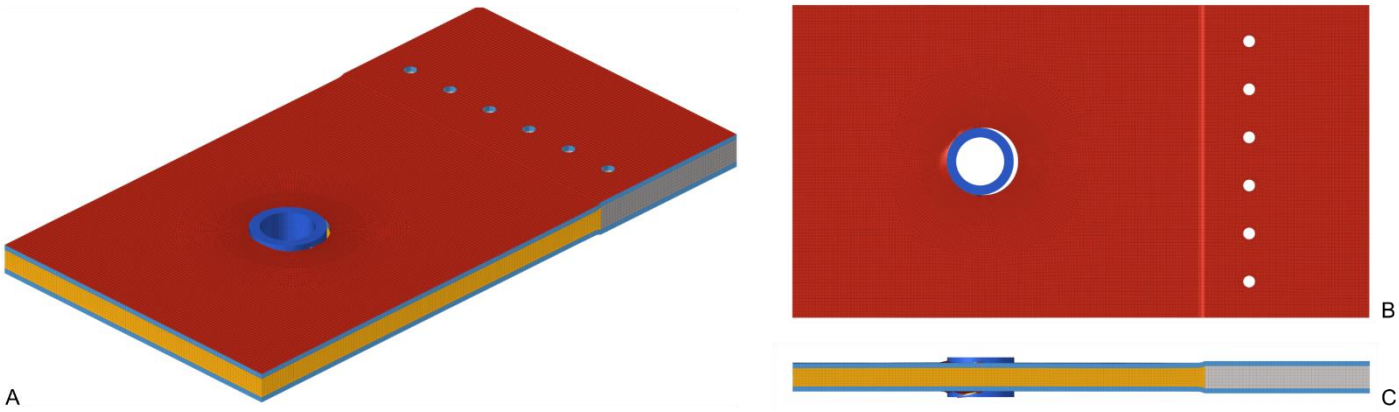

Figure 11. The numerical fracture surface of simple composite joint model. (**A**) Fracture axonometry. (**B**,**C**) Fracture surface.

The characteristic force-displacement curve of the simple composite joint is reported in Figure 9. Both curves are comparable, and no remarkable differences are revealed. The internal contact load exactly follows the global failure load of the simple specimen. The absence of steel reinforcement increases the localization of the damage and the initiation of the bearing fracture mode in the contact region, as in Figure 11, but no evidence of a propagation of such mode of fracture is determined, as revealed in the experimental test shown in Figure 5B. This is probably due to the compressive guided mode of failure in the contact zone that requires a consistent and correct definition of compressive material properties, both in the elastic range and in the post-failure condition. The data introduced in the simulation were instead extrapolated by a generic database, so a certain dispersion in results was expected when comparing the experimental failure load of about 40 kN to the numerical one, as in Table 9. The post-failure parameters (ERODS and $SLIM_{xx}$) characteristic of MAT58 could also play a role in the correct identification of the failure mode; a correct calibration seems to be required on the basis of the real characterization of the material properties. An extensive characterization of the material properties seems necessary with a deeper calibration of the principal post-failure numerical parameters available in the proposed LS-DYNA material models. The adoption of the same erosion parameters for the two situations could also be too stringent assumption and a more detailed investigation on its sensitivity to the numerical simulation will need to be performed as a subject for future research activities.

The punctual strain values obtained in the proposed numerical model at 20 kN of tensile load for both composite specimens were reported in Polla et al. [12] against the results proposed by Frulla et al. [1], as summarized in Figures 12 and 13. The deformation

local path is in good agreement with the literature results for SG 3–4 and SG 5. The strain field differences between the advanced and simple composite joints have also been found for numerical SG 1–2. However, a slight difference between the results found by Frulla et al. and the present value was observed. The lack of a complete material characterization was the major effect that could influence the obtained numerical results. The global strain field maps between the advanced and simple composite joints are compared in Figure 14. The picture reports the localized longitudinal strain map obtained at 20 kN of tensile load in the external composite ply of the proposed joints. A certain level of strain-concentration is evident near the contact area and at the hole edges in the simple configuration (B). A large reduction in the hole edge concentration and homogeneous distribution in the entire external surface can be evaluated with the application of the advanced solution (A). Reduced differences have been found in comparison to the literature results. A qualitative view of the longitudinal strain distribution was proposed. An extended evaluation of stress-strain is proposed for future work.

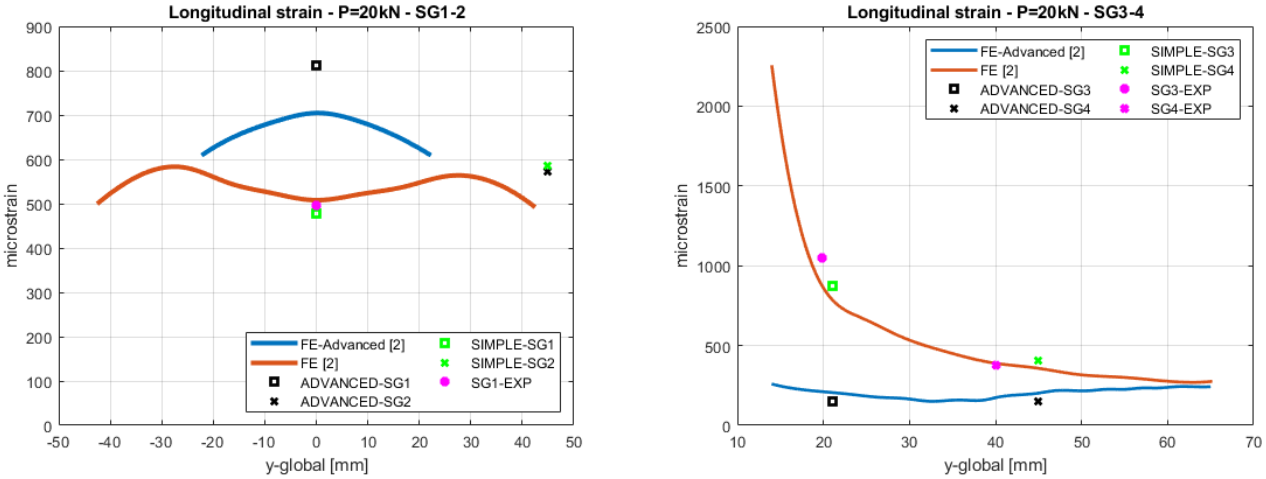

Figure 12. Strain comparison for SG 1–2 and 3–4 between static FE [2] and present numerical simulation. Experimental strain values are from Frulla et al. [1].

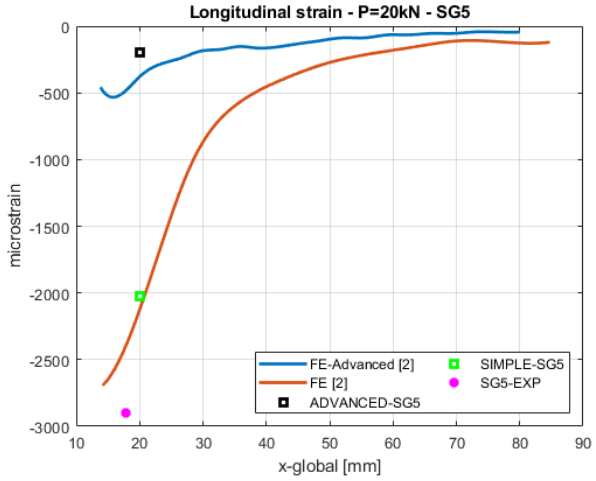

Figure 13. Strain comparison for SG 5 between static FE [1] and present numerical simulations. Experimental strain values are from Frulla et al. [1].

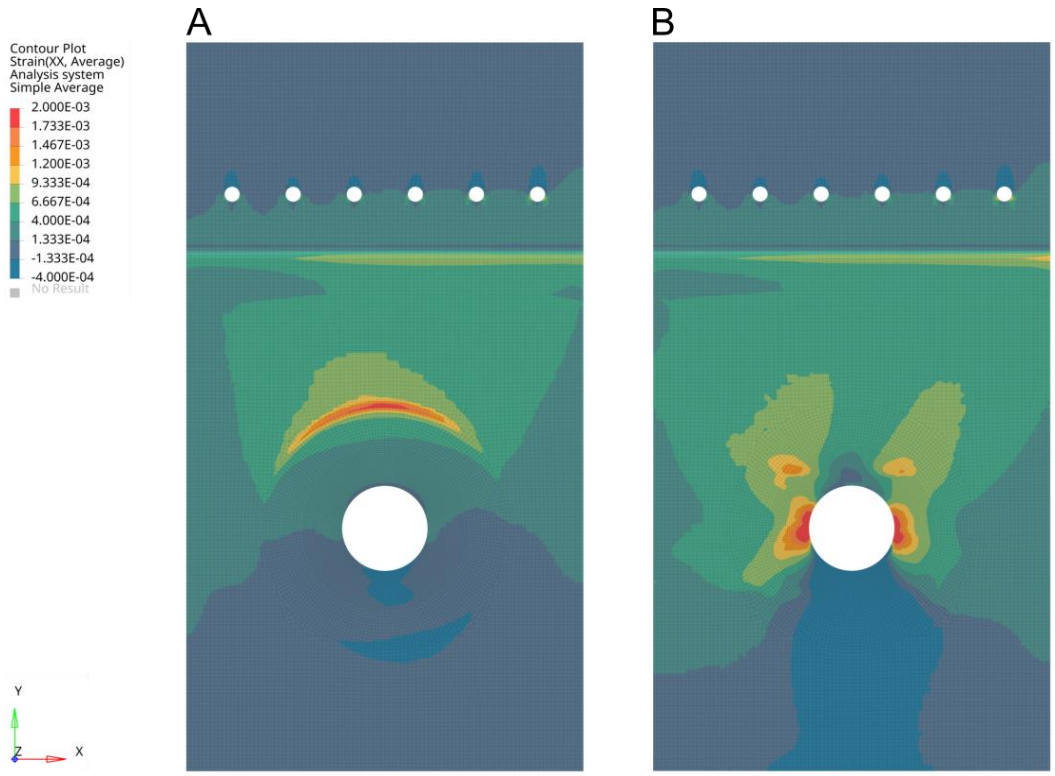

Figure 14. An external qualitative view of the longitudinal strain distribution of the advanced and simple joint (**A**) first-ply longitudinal strain of the advanced composite face under 20 kN (**B**) first-ply longitudinal strain of the simple composite face under 20 kN.

6. Conclusions

A complete new and significant high-fidelity shell-cohesive numerical procedure was detailed to establish the mechanical response (elastic, plastic, and failure) of the composite pin-loaded joint configuration proposed by Frulla and Romeo, and a comparison between experimental and numerical campaign was offered. The advanced joint was designed to demonstrate an improvement in loading strength that eliminates the typical bearing failure of a simple composite configuration. Numerical simulations demonstrated a satisfactory correlation with the experimental results in the advanced joint case. Both strain distribution in pre-failure condition, failure load level, and post-failure fracture propagation confirmed the validity of the presented methodology and procedure. In particular, the proposed numerical model properly evaluated and defined the non-linear behavior observed in correspondence to the failure condition for the same case under the control-displacement loading phase. Reference material and numerical parameters were proposed for the selected formulations available in LS-DYNA R11.1. The best numerical results obtained from the described numerical campaign were reported and compared with the experimental results. The average peak loads obtained after the calibration process of the erosion parameter demonstrated that the *MAT_LAMINATED_COMPOSITE_FABRIC material model could correctly reproduce the failure mechanisms and strength limit experimentally observed for the advanced configuration. The simple composite joint was also compared with experimental evidence. The strain distribution in pre-failure conditions demonstrated a satisfactory correlation with the experimental one, but high failure load level was numerically observed. The compressive guided failure condition in the contact point was considered to be a critical aspect in obtaining a consistent numerical/experimental correlation. Therefore, material compressive properties should be carefully selected after specific material characterization campaigns instead of being extracted from a general database. It is also important for post-failure propagation and fracture mode definition whether the typical bearing failure has been correctly identified

by numerical models. The simple composite joint simulation showed that the calibrated post-failure parameters must be selected to simulate real material behavior. A structured evaluation is required to select the appropriate numerical erosion and post-failure residual strength parameters according to the real fracture mode. Preliminary test-analysis correlation indicated that the selected modeling technique adopted for this study could be used to predict experimental results with a reduced computational cost when compared to the significant number of laboratory tests on composite sandwich joints.

Author Contributions: Conceptualization, G.F., E.C. and R.D.; Methodology, A.P., G.F. and E.C.; Software, A.P.; Validation, G.F.; Investigation, A.P. and G.F.; Resources, P.M.; Data curation, G.F.; Writing—original draft, A.P. and G.F.; Supervision, G.F., E.C., R.D. and P.M. All authors have read and agreed to the published version of the manuscript.

Funding: This research received no external funding.

Institutional Review Board Statement: Not applicable.

Informed Consent Statement: Not applicable.

Data Availability Statement: Not applicable.

Conflicts of Interest: The authors declare no conflicts of interest.

References

1. Romeo, G.; Frulla, G. HELIPLAT®: Aerodynamic and structural analysis of HAVE solar powered platform. In Proceedings of the 1st UAV Conference 2002, Reston, VA, USA, 20–23 May 2002.
2. Frulla, G.; Romeo, G. Numerical/experimental structural characterization of composite advanced joints for HALE-UAV platforms. *Compos. Part B Eng.* **2008**, *39*, 656–664. https://doi.org/10.1016/j.compositesb.2007.06.003.
3. Romeo, G.; Frulla, G. Experimental behavior of Composite Advanced Joint under cyclic loads. *Struct. Integr. Adv. Aircr. Life Ext. Curr. Fleets-Lesson Learn. 50 Yers Comet Accid.-23rd ICAF Symp. Proc.* **2005**, *2*, 507–517.
4. Romeo, G.; Frulla, G. Bearing strength of bolted joints in CFRP wing fittings. In Proceedings of the 23rd congress of the international council of the aeronautical sciences (ICAS), Toronto, ON, Canada, 8–13 September 2002; pp. 8–13.
5. Wang, H.-S.; Hung, C.-L.; Chang, F.-K. Bearing Failure of Bolted Composite Joints. Part I: Experimental Characterization. *J. Compos. Mater.* **1996**, *30*, 1284–1313. https://doi.org/10.1177/002199839603001201.
6. Wright, R.J.; Johnson, W.S.; Ahmad, H. Bolt Bearing Behavior of Highly Loaded Composite Joints at Elevated Temperatures with and without Clamp-up. *Compos. Struct.* **1997**, *6*, 9.
7. Haufe, A.; Cavariani, S.; Liebold, C.; Usta, T.; Kotzakolios, T.; Giannaros, E.; Kostopoulos, V.; Hornig, A.; Gude, M.; Djordjevic, N.; et al. On Composite Model Calibration for Extreme Impact Loading Exemplified on Aerospace Structures. In Proceedings of the 16th International LS-DYNA ® Users Conference, Virtual, 10–11 June 2020; p. 14.
8. Hunziker, K.J.; Pang, J.; Pereira, M.; Melis, M.; Rassaian, M. NASA ACC High Energy Dynamic Impact Methodology and Outcomes. In Proceedings of the 2018 AIAA/ASCE/AHS/ASC Structures, Structural Dynamics, and Materials Conference, Kissimmee, FL, USA, 8–12 January 2018. https://doi.org/10.2514/6.2018-1700.
9. Justusson, B.; Pang, J.; Molitor, M.; Rassaian, M.; Rosman, R. An Overview of the NASA Advanced Composites Consortium High Energy Dynamic Impact Phase II Technical Path. In Proceedings of the AIAA Scitech 2019 Forum, San Diego, CA, USA, 7–11 January 2019. https://doi.org/10.2514/6.2019-2052.
10. Cestino, E.; Romeo, G.; Piana, P.; Danzi, F. Numerical/experimental evaluation of buckling behaviour and residual tensile strength of composite aerospace structures after low velocity impact. *Aerosp. Sci. Technol.* **2016**, *54*, 1–9. https://doi.org/10.1016/j.ast.2016.04.001.
11. Polla, A.; Piana, P.; Cestino, E.; Frulla, G. Delamination and Fracture Modeling Techniques for Shell Composite Structures in LS-DYNA®. In Proceedings of the 13th European LS-DYNA Conference, Ulm, Germany, 5–7 October 2021; p. 12.
12. Polla, A.; Frulla, G.; Cestino, E.; Das, R.; Marzocca, P. Numerical and Experimental structural characterization of composite advanced joint for ultra-light aerospace platform. In Proceedings of the 33rd ICAS Congress, Stockholm, Sweden, 4–9 September 2022.
13. Frulla, G.; Cestino, E. Design, manufacturing and testing of a HALE-UAV structural demonstrator. *Compos. Struct.* **2008**, *83*, 143–153. https://doi.org/10.1016/j.compstruct.2007.04.008.
14. Hexcel® HexPly® 954-6 Curing Cyanate Resin, M40J Fiber. Available online: https://www.matweb.com/search/datasheet.aspx?matguid=446a4c9dc9fe403fbdb0ffd5867a625b&ckck=1 (accessed on 15 December 2022).
15. Evonik Rohacell® 51 Polymethacrylimide (PMI) Rigid Foam Sheet. Available online: http://www.matweb.com/search/datasheet.aspx?matguid=d59129af94c4448783ee193fba1ff102 (accessed on 15 December 2022).
16. ARALDITE® 2015-1—HUNTSMAN. Available online: https://www.huntsman.com/products/araldite2000/araldite-2015-1 (accessed on 15 December 2022).

17. Livermore Software Technology, LS-DYNA® Keyword User's Manual, Volume II, LS-DYNA R13. 2021. Available online: www.lstc.com (24 September 2021).
18. Livermore Software Technology, LS-DYNA® Keyword User's Manual, Volume I, LS-DYNA R13. 2021. Available online: www.lstc.com (27 September 2021).
19. Obradovic, J.; Boria, S.; Belingardi, G. Lightweight design and crash analysis of composite frontal impact energy absorbing structures. *Compos. Struct.* **2012**, *94*, 423–430. https://doi.org/10.1016/j.compstruct.2011.08.005.
20. Hinton, M. Predicting failure in composite laminates: The background to the exercise. *Compos. Sci. Technol*. **1998**, *58*, 1001–1010. https://doi.org/10.1016/S0266-3538(98)00074-8.
21. Soden, P. A comparison of the predictive capabilities of current failure theories for composite laminates. *Compos. Sci. Technol.* **1998**, *58*, 1225–1254. https://doi.org/10.1016/S0266-3538(98)00077-3.
22. LLorca, J.; González, C.; Molina-Aldareguía, J.M.; Segurado, J.; Seltzer, R.; Sket, F.; Rodríguez, M.; Sádaba, S.; Muñoz, R.; Canal, L.P. Multiscale Modeling of Composite Materials: A Roadmap Towards Virtual Testing. *Adv. Mater.* **2011**, *23*, 5130–5147. https://doi.org/10.1002/adma.201101683.
23. Gomez, L.; Olivares, G.; Kona, A.; Bhasin, A.; Gomez, A.; Keshavanarayana, S.; Pang, J.; Molitor, M.; Rassaian, M. Evaluation of Ls-Dyna MAT162 for Modeling Composite Fastener Joints for High Rates of Loading. In Proceedings of the AIAA Scitech 2019 Forum, San Diego, CA, USA, 7–11 January 2019. https://doi.org/10.2514/6.2019-2058.
24. Girolamo, D.; Davila, C.G.; Leone, F.A.; Lin, S.-Y. Cohesive Laws and Progressive Damage Analysis of Composite Bonded Joints, a Combined Numerical/Experimental Approach. In Proceedings of the 56th AIAA/ASCE/AHS/ASC Structures, Structural Dynamics, and Materials Conference, Kissimmee, FL, USA, 5–9 January 2015. https://doi.org/10.2514/6.2015-1578.
25. Gerendt, C.; Dean, A.; Mahrholz, T.; Rolfes, R. On the progressive failure simulation and experimental validation of fiber metal laminate bolted joints. *Compos. Struct.* **2019**, *229*, 111368. https://doi.org/10.1016/j.compstruct.2019.111368.
26. Matzenmiller, A.; Lubliner, J.; Taylor, R.L. A constitutive model for anisotropic damage in fiber-composites. *Mech. Mater.* **1995**, *20*, 125–152. https://doi.org/10.1016/0167-6636(94)00053-0.

Disclaimer/Publisher's Note: The statements, opinions and data contained in all publications are solely those of the individual author(s) and contributor(s) and not of MDPI and/or the editor(s). MDPI and/or the editor(s) disclaim responsibility for any injury to people or property resulting from any ideas, methods, instructions or products referred to in the content.